



City Research Online

City, University of London Institutional Repository

Citation: Stefanitsis, D., Koukouvinis, F. ORCID: 0000-0002-3945-3707, Nikolopoulos, N. and Gavaises, M. ORCID: 0000-0003-0874-8534 (2020). Numerical investigation of the aerodynamic droplet breakup at Mach numbers >1 . *Journal of Energy Engineering*,

This is the accepted version of the paper.

This version of the publication may differ from the final published version.

Permanent repository link: <https://openaccess.city.ac.uk/id/eprint/24574/>

Link to published version:

Copyright and reuse: City Research Online aims to make research outputs of City, University of London available to a wider audience. Copyright and Moral Rights remain with the author(s) and/or copyright holders. URLs from City Research Online may be freely distributed and linked to.

City Research Online:

<http://openaccess.city.ac.uk/>

publications@city.ac.uk

Numerical investigation of the aerodynamic droplet breakup at Mach numbers >1

Affiliations

Dionisis Stefanitsis^{*1}, Phoivos Koukouvinis², Nikolaos Nikolopoulos³, Manolis Gavaises⁴

¹Research fellow at the Centre for Research and Technology Hellas/Chemical Process and Energy Resources Institute (CERTH/CPERI), Egialeias 52, Marousi, Greece. E-mail: stefanitsis@certh.gr

²Research fellow at the City University London, School of Engineering and Mathematical Sciences, Northampton Square, EC1V 0HB London, UK. E-mail: Foivos.Koukouvinis.1@city.ac.uk

³Researcher B at the Centre for Research and Technology Hellas/Chemical Process and Energy Resources Institute (CERTH/CPERI), Egialeias 52, Marousi, Greece. E-mail: n.nikolopoulos@certh.gr

⁴Professor at the City University London, School of Engineering and Mathematical Sciences, Northampton Square, EC1V 0HB London, UK. E-mail: M.Gavaises@city.ac.uk

Abstract

The present work examines numerically the breakup of water droplets exposed to gas flows at Mach numbers $Ma > 1$, which resemble the ambient conditions encountered in the injection systems of scramjet (supersonic combustion ramjet) engines. A CFD model is utilized which solves the compressible Navier-Stokes equations, the energy equation, the mass conservation in volume fraction form (volume of fluid method) along with two equations of state to model the density variations of the two phases. In addition, a coupled VOF/Lagrange model is employed to capture the appearance of micro-droplets, which are smaller than the smallest grid cell. As a first step, a 2-dimensional planar simulation (water column) is performed at conditions of $Ma = 1.47$ in order to validate the numerical model; its results are compared against published experimental and numerical data. Good agreement

25 is observed for the temporal evolution of droplet shape, the streamwise deformation, the leading-
26 edge displacement as well as the shock wave reflection. Subsequently, the validated model is utilized
27 to perform a 3-D simulation at $Ma=1.23$, which corresponds to the conditions of previous experimental
28 studies, and its results are compared against the experimental data as well as the results from previous
29 numerical studies, showing good agreement. Furthermore, surface instabilities are observed at the
30 droplet surface initiated by interfacial instabilities due to the shearing effect and the interaction with
31 the shock-wave, pertaining to Kelvin-Helmholtz and Rayleigh-Taylor instabilities, despite the stabilising
32 contribution of surface tension; viscosity effects are found to play an insignificant role.

33

34 **Keywords**

35 Droplet breakup; shock wave; high Mach number; CFD; surface instabilities;

36

37 **Introduction**

38 The breakup of droplets exposed to Mach numbers >1 has received a lot of attention recently due to
39 its application in supersonic combustion ramjet (scramjet) engines (Liu et al. 2018). These types of
40 engines utilize the supersonic vehicle speed to compress the incoming airflow without the use of a
41 compressor. Other non-dimensional numbers that are usually utilised for classifying the breakup of
42 droplets are the Weber (We), Ohnesorge (Oh) and Reynolds (Re) numbers as well as the density (ϵ)
43 and viscosity ratios (N) of the two phases (Guildenbecher et al. 2009); these are calculated based on
44 the post-shock properties as:

45

$$We = \frac{\rho_g U_{sh}^2 D_0}{\sigma} \quad Oh = \frac{\mu_L}{\sqrt{\rho_L \sigma D_0}} \quad Re = \frac{\rho_g U_{sh} D_0}{\mu_g} \quad \epsilon = \frac{\rho_L}{\rho_g} \quad N = \frac{\mu_L}{\mu_g} \quad (1)$$

46

47 The breakup timescale can be also approximated by the non-dimensional correlation proposed by
48 (Nicholls and Ranger 1969) ($t^* = t/t_{shear}$):

49

$$t_{shear} = \frac{D_0}{U_{sh}} \sqrt{\varepsilon} \quad (2)$$

50

51 Experimental studies on the breakup of droplets at high Ma numbers were performed as early as 1958,
52 when (Engel 1958) conducted experiments with water droplets exposed to an air flow of Mach number
53 ranging from 1.3 up to 1.7. She observed the formation of a mist at the periphery of the droplet and
54 also measured its breakup time. Later, Boiko and co-workers (Boiko et al. 1987; Boiko and Poplavski
55 2009) performed experiments with droplets of various liquids (water, alcohol, glycerine, and tridecane)
56 interacting with flows of Helium and air at Mach numbers ranging from 0.15 up to 4, and Weber
57 numbers greater than 400. They observed that the disintegration of the droplets originates from their
58 surface (core or periphery) and they attributed it to the appearance of Rayleigh-Taylor and Kelvin-
59 Helmholtz (KH) instabilities. The research group of K. Takayama (Wierzba and Takayama 1988; Yoshida
60 and Takayama 1990) examined experimentally the breakup of water droplets in an air flow of Ma
61 number ranging from 1.3 up to 1.56 and We number between 600 and 760. They divided the breakup
62 process into four stages: i) disruption of the liquid surface, ii) droplet deformation and initiation of the
63 formation of micro-droplets, iii) continuous stripping of micro-droplets until deformation reaches
64 maximum, and iv) remaining parent droplet breaks into large fragments. Joseph and co-workers
65 (Joseph et al. 2002; Joseph et al. 1999) examined experimentally the breakup of Newtonian and
66 viscoelastic droplets due to the interaction with a shock-wave of Mach number from 2 up to 3.03, We
67 number from 11700 up to 169000 and Oh number from 0.002 to 82.3. They encountered bag and bag-
68 and-stamen breakup modes even at such high We numbers, owing to the high Oh of the viscoelastic
69 liquids. Moreover, they developed a simplified theory to predict the critical wave length and growth
70 rate of the Rayleigh–Taylor (RT) instabilities.

71 Theofanous and co-workers (Theofanous and Li 2008; Theofanous et al. 2012) conducted experiments
72 with water and viscous liquid droplets (silicon oil, glycerol and tri-butyl phosphate) suddenly exposed
73 to supersonic gas streams. The examined Ma numbers ranged from 1.1 up to 3.5, the We numbers
74 from 12 up to $2 \cdot 10^5$ and the Oh numbers from 0.0012 up to 540. They utilized the laser-induced
75 fluorescence technique to visualize the droplets and questioned the results of the previous
76 experiments, which used the shadowgraph method. Specifically, they attributed the breakup of the
77 droplets at We numbers greater than 1000 to the shear induced entrainment (SIE) instead of the
78 previously thought Rayleigh–Taylor piercing (RTP); they concluded that the latter occurs at We
79 numbers in the range of 10 up to 100. In addition, they questioned the existence of the catastrophic
80 breakup regime and stated that it is a mirage of the shadowgraph technique. Finally, they observed
81 that Kelvin-Helmholtz instabilities play an important role in the breakup of viscous liquids. Later, (Yi et
82 al. 2017) studied experimentally and numerically the early-stage deformation of water droplets in a
83 supersonic air flow of Mach number ranging from 1.39 up to 1.90, and We number in the order of 10^3 -
84 10^4 . They identified two mechanisms that are responsible for the droplet deformation at the early-
85 stages, namely: i) pressure mechanism, which is responsible for the droplet flattening, and ii) shear
86 mechanism, which is responsible for the formation of the small rings and bulges. Recently, (Hébert et
87 al. 2019) studied experimentally and numerically in 2-dimensions, using an in-house code called
88 Hesione, the breakup of water droplets exposed to gas flows of $Ma=4.2-4.6$ and $We>10^5$. They
89 encountered the catastrophic breakup mode and divided the breakup process into three steps: i)
90 droplet flattening, ii) fragmentation initiation at the outer rim of the droplet, and iii) droplet takes the
91 shape of a filament aligned with the flow.

92 Turning now to the numerical studies of droplet breakup at high Ma numbers, (Surov 1995) was one
93 of the first to study numerically the interaction of a shock wave with a liquid droplet. He investigated
94 water and glycerine droplets at Ma numbers ranging from 3 to 10 and observed that an increase in
95 liquid viscosity leads to a slight decrease in the rate of deformation of the droplet, while the liquid

96 density affects substantially the droplet deformation and displacement. Chang and co-workers (Chang
97 et al. 2013; Liou et al. 2009) performed 2-D axisymmetric simulations using the AUSM+- numerical
98 scheme (Chang and Liou 2007) of water and glycerol droplets exposed to an airflow of Ma number in
99 the range of 0.29 up to 3, We number from 520 up to $5.4 \cdot 10^4$ and Oh number up to 1.9. They identified
100 the RTP and SIE breakup modes and attributed each breakup mode to the Rayleigh–Taylor and Kelvin-
101 Helmholtz instabilities, respectively, similar to the experimental studies of (Theofanous and Li 2008;
102 Theofanous et al. 2012). (Xiao et al. 2017) used the coupled Level Set with Volume of Fluid (CLSVOF)
103 interface tracking method to study the breakup of tributylphosphate droplets in supersonic flows. With
104 a fixed Mach number equal to 3, they investigated the effect of density ratio, which ranges from 18,544
105 up to 667,577 and We number in the range of 15 to 75. They encountered the bag, bag-and-stamen
106 and multimode breakup modes and concluded that the Weber numbers separating the different
107 breakup modes, as well as the breakup initiation time, are higher in supersonic flows compared to
108 those of the subsonic ones. (Guan et al. 2018) used the five equation model (Euler equations coupled
109 with the stiffened gas equation of state (EoS)) to study the axisymmetric breakup of water, gelatine,
110 fat and dodecane droplets subjected to an air shock-wave. They examined Ma numbers in the range
111 of 1.39 up to 3.9 and We numbers of the order of 10^3 ; they observed that there is a saddle point (point
112 of zero velocity) inside the droplet; its position was found to depend on the Ma number and proposed
113 a simplified theory to predict it. (Meng and Colonius 2018; Meng 2016) also used the five-equation
114 model of (Allaire et al. 2002) to simulate in 3-dimensions the breakup of a water droplet exposed to
115 an air flow of $Ma=1.47$ and $We=780$. They compared qualitatively their results with those of the
116 experimental study of (Theofanous et al. 2004); good agreement was found regarding the initial
117 droplet deformation into a muffin-like shape, as well as the following disintegration into two liquid
118 sheets, in agreement with (Liu and Reitz 1997). Moreover, KH instabilities were observed pertaining to
119 the SIE breakup mode, which was also reported in (Theofanous et al. 2004). Nevertheless, the micro-
120 mist appearing at the periphery of the droplet was not captured in that study. For the same conditions,

121 (Kaiser et al. 2017) used the Level Set (LS) method coupled with the compressible Euler equations and
122 the stiffened-gas EoS to simulate the breakup of a water droplet exposed to an air flow. They
123 performed 2-D (water column) and 3-D simulations and confirmed the results of (Meng and Colonius
124 2018; Meng 2016) for the existence of two liquid sheets during the breakup of the droplet, while they
125 also observed a third sheet upstream of the droplet; however, they stated that 3-D simulations with
126 higher resolution are necessary to confirm this observation. Finally, (Liu et al. 2018) also utilized the
127 five-equation model and performed 3-D simulations of water droplet breakup in an airflow of Ma
128 number in the range of 1.2 up to 1.8. They presented qualitative and quantitative results for the droplet
129 drift, velocity and acceleration and defined three stages of the breakup process in the SIE regime: i)
130 surface instability, ii) droplet flattening, and iii) entrainment from the liquid sheet.

131 The current work investigates the breakup of a water droplet exposed to a flow of Ma ranging from
132 1.23 up to 1.47 with the aim to capture for the first time in CFD simulations (to the author's best of
133 knowledge) the appearance of micro-droplets stripped from the parent droplet. A numerical model is
134 utilized which solves the compressible Navier-Stokes equations, the energy equation, the conservation
135 of the volume fraction (VOF method) along with two equations of state to model the density variations
136 of the two fluids. Furthermore, a coupled VOF/Lagrange model is employed to capture the appearance
137 of micro-droplets, which switches from VOF to Lagrange models when certain user-defined criteria are
138 met. 2-D planar and 3-D simulations are performed in the commercial software FLUENT v19.2 and
139 qualitative and quantitative results are presented and compared with published experimental and
140 numerical data.

141 The paper is structured as follows: in the following chapter the numerical model is presented, followed
142 by a chapter with the computational setup and examined conditions. Next, the results of the
143 simulations are presented regarding the model validation with the 2-D planar domain as well as the 3-
144 D simulation using the VOF/Lagrange model. In the last section of the paper the main conclusions of
145 the current work are presented.

146

147 Numerical model

148 Flow equations and volume of fluid (VOF) method

149 The CFD model for the aerodynamic breakup of droplets solves the mass and energy conservation
150 equations as well as the Navier-Stokes equations coupled with the Volume of Fluid (VOF) methodology
151 of (Hirt and Nichols 1981) for capturing the interface between liquid and gas.

152 A single continuity equation is solved for both phases (no mass sources are taken into consideration)

153

$$\frac{\partial \rho}{\partial t} + \nabla \cdot (\rho \vec{u}) = 0 \quad (3)$$

154

155 , as also a single momentum equation; the resulting velocity field is shared among the phases:

156

$$\frac{\partial(\rho \vec{u})}{\partial t} + \nabla \cdot (\rho \vec{u} \vec{u}) = -\nabla P + \nabla \cdot [\mu(\nabla \vec{u} + \nabla \vec{u}^T)] + \rho \vec{g} + \vec{F}_{vol} \quad (4)$$

157

158 The surface tension forces are included in the momentum equation by using the Continuum Surface
159 Stress (CSS) model of (Lafaurie et al. 1994). In the CSS model the volumetric force is calculated as

160

$$\vec{F}_{vol} = \nabla \cdot \left[\sigma \left(|\vec{n}| I - \frac{\vec{n} \otimes \vec{n}}{|\vec{n}|} \right) \right], \vec{n} = \nabla \alpha \quad (5)$$

161

162 The volume fraction α is defined as:

163

$$\alpha = \frac{\text{Volume of liquid phase}}{\text{Total volume of the control volume}} \quad (6)$$

164

165 , where the α -function is equal to:

- 166 • 1, for a point inside liquid phase.
- 167 • 0, for a point inside gas phase.
- 168 • $0 < \alpha < 1$, for a point inside the transitional area of the two phases, the interface.

169

170 The transport equation for the liquid volume fraction, since no mass sources are taken into
 171 consideration, is

172

$$\frac{\partial \rho_L \alpha}{\partial t} + \nabla \cdot (\rho_L \alpha \vec{u}) = 0 \quad (7)$$

173

174 The values of the density ρ and viscosity μ are calculated using linear interpolation between the two
 175 phases weighted with the volume fraction α :

176

$$\rho = \alpha \rho_L + (1 - \alpha) \rho_g \quad (8)$$

177

$$\mu = \alpha \mu_L + (1 - \alpha) \mu_g \quad (9)$$

178

179 The energy equation is given in eq. (10) for a flow without species and negligible viscous energy
 180 dissipation; preliminary 2D simulations using the viscous heating option of FLUENT (viscous heating
 181 terms in the energy equation are enabled) have shown that the droplet deformation as well as the
 182 displacement experience negligible change when the viscous heating effect is taken into account.

183

$$\frac{\partial(\rho E)}{\partial t} + \nabla \cdot [\vec{u}(\rho E + P)] = \nabla \cdot (k \nabla T) \quad (10)$$

184

185 , where the energy E is given by

186

$$E = h - \frac{P}{\rho} + \frac{v^2}{2} \quad (11)$$

187

188 , with the sensible enthalpy h calculated in its general form (Sonntag et al. 2008) by

189

$$h = \int_{T_{ref}}^T C_p dT + \int_{p_1}^{p_2} \left[v - T \left(\frac{\partial v}{\partial T} \right)_p \right] dp \quad (12)$$

190

191 , where the specific volume is $v = 1/\rho$. For the ideal gas (air or nitrogen in this work) the second term

192 of the right-hand-side of eq. (12) becomes equal to zero, while for an incompressible material it

193 becomes equal to $\frac{P - P_{ref}}{\rho}$. In the case of weakly compressible materials, such as liquids, exposed to the

194 pressure variations encountered here, the difference between incompressible and weakly

195 compressible (e.g. Tait EoS eq. (13)) calculation of liquid enthalpy are negligible; preliminary

196 calculations showed that the error is less than 1% for pressures up to 450 bar.

197

$$h = \int_{T_{ref}}^T C_p dT + \frac{B \cdot n \left(1 + \frac{P - P_{ref}}{B} \right)^{\frac{n-1}{n}} - B \cdot n}{(n-1)\rho_{ref}} \quad (13)$$

198

199 , where B is a parameter and n is a material exponent equal to 7.15 for water (Ivings et al. 1998).

200

201 **Equations of state (EoS) and rest of fluid properties**

202 For the cases with large density variations, such as those encountered at Mach numbers > 1 , the
203 density of each fluid is given as function of its temperature and pressure using an equation of state for
204 each phase: i) for the gas phase the ideal gas law is utilized ($\rho=PMW_{gas}/RT$), while for the liquid phase
205 the Tait EoS is used (eq. (14)):

206

$$\left(\frac{\rho}{\rho_0}\right)^n = \frac{K}{K_0} \quad (14)$$

207

208 , where K is the bulk modulus, which is a measure of the compressibility of a liquid; it is given in its
209 general form by:

210

$$K = -V \frac{dP}{dV} \quad (15)$$

211

212 For the examined conditions of the current work ($T \approx 293.15\text{K}$ and P ranges from 1.01325 bar up to ~ 2.8
213 bar - see section with the computational setup) the bulk modulus can be assumed to vary linearly with
214 pressure (Gor et al. 2016): $K=K_0+n\Delta p$, with $\Delta p=p-p_0$ and $n=7.15$ for water (Ivings et al. 1998), with
215 reference values as: $P_0=101325$ Pa, $\rho_0=998.2$ kg/m³, $K_0=2.2 \cdot 10^9$ Pa (Menon 2014). It should be noted
216 that for such small changes in the temperature ($\Delta T < 1$ K) and pressure ($\Delta P \sim 1.8$ bar) the density of water
217 changes less than 1% and therefore not much difference is expected in the results with the use of
218 constant density; however, this was not known a priori. For the same reason, the rest of fluid
219 properties (surface tension, viscosity, heat capacity and thermal conductivity) are taken constant for
220 the liquid water at the initial temperature of 293.15 K. Preliminary CFD simulations using variable
221 properties for water based on (Lemmon 2013; Wagner and Pruiß 2002) and the tabulated method of
222 (Koukouvinis; et al. 2020) have shown that the droplet deformation in both axes changes less than 1%,

223 while the leading edge displacement is overestimated by a maximum of 10% at the final stages of the
224 simulation with the constant properties approach, probably due to difference in the fluid viscosity. For
225 the gas phase (air or nitrogen), which has large variations in the pressure and temperature, the heat
226 capacity and thermal conductivity are taken as functions of temperature, using the polynomial
227 functions of (Perry and Green 1999). Finally, the viscosity of gas is found using the Sutherland's law
228 (Sutherland 1893).

229

230 **VOF-to-DPM model**

231 In the VOF-to-DPM model the liquid volume fraction of a cell is converted into Lagrangian particles
232 (droplets), when certain user-specified criteria are met. In order to avoid spurious momentum sources,
233 an equal volume of gas is created in the VOF solution to maintain the volume conservation. The criteria
234 for transition from VOF to DPM in a cell are: i) the volume-equivalent sphere diameter should be within
235 a specified range, which for this work is chosen between zero and the diameter of a particle that would
236 occupy half the volume of an interface cell; this ensures that the stripping of micro-droplets will initiate
237 from the droplet interface when it is close to its initial spherical shape (a lower number would not
238 allow that since the domain has a wedge-like shape and the volume of the cells increases radially).
239 However, this choice affects the size of the stripped particles, as discussed in sub-section "Description
240 of fluid flow" of the 3-D simulation. The second criterion (ii) is that the asphericity should be below 0.5
241 (the value of zero corresponds to perfect spheres, while the higher it is the more the shape deviates
242 from that of sphere); the higher the value of the asphericity the higher the number of cells that are
243 elected for conversion (in (Bo Shen 2019) they found that a value of asphericity equal to 0.5
244 corresponded to 95% of the mass of the spray being converted into Lagrangian particles). After the
245 particles-droplets have been created, their trajectory is tracked using the force balance on each of
246 them separately, as given by eq. (16):

247

$$m_d \frac{d\vec{u}_d}{dt} = m_d \frac{\vec{u} - \vec{u}_d}{\tau_r} + m_d \frac{\vec{g}(\rho_d - \rho_g)}{\rho_d} + \vec{F} \quad (16)$$

248

249 The first term on the right-hand side is the term of the drag force, the second term is the gravity force,
 250 which is negligible compared to the aerodynamic force, and the third one includes all other forces
 251 (virtual mass, pressure gradient etc), which in the current work of high density ratio ($\rho_d/\rho_g \gg 1$) are
 252 considered negligible. τ_r is the droplet relaxation time calculated by:

253

$$\tau_r = \frac{\rho_d d_d^2}{18\mu} \frac{24}{C_D Re} \quad (17)$$

254

255 , with Re being the relative Reynolds number given by:

256

$$Re = \frac{\rho_d d_d |\vec{u}_d - \vec{u}|}{\mu} \quad (18)$$

257

258 and C_d the drag coefficient, calculated using the spherical drag law as:

259

$$C_d = a_1 + \frac{a_2}{Re} + \frac{a_3}{Re} \quad (19)$$

260

261 , where the coefficients α_1 , α_2 and α_3 are given in (Morsi and Alexander 1972).

262

263 **Computational setup and examined conditions**

264 **2-D simulation of water column breakup (model validation)**

265 The CFD model has been utilized and validated in previous works of the authors for a number of
266 applications; among them are the free fall of a droplet (Malgarinos et al. 2015), the droplet
267 impingement on a flat wall (Malgarinos et al. 2014) or a spherical particle (Malgarinos et al. 2016;
268 Malgarinos et al. 2017; Malgarinos et al. 2017), the aerodynamic breakup of droplets and droplet
269 clusters at low Ma numbers (G. Strotos 2015; Stefanitsis et al. 2017; Stefanitsis et al. 2017; Stefanitsis
270 et al. 2018; Stefanitsis et al. 2019; Stefanitsis et al. 2018; Stefanitsis et al. 2019; Strotos et al. 2016;
271 Strotos et al. 2016; Strotos et al. 2016) and the droplet evaporation (Strotos et al. 2016; Strotos et al.
272 2016; Strotos et al. 2016). In this work, its validation is extended to the case of droplet breakup at high
273 Ma numbers. For this reason, a 2-D planar (column) simulation is performed in the computational
274 domain of Figure 1. The shock wave is initialized as a step change in pressure, temperature and velocity
275 (pink color in the figure), which are calculated based on the desired Ma number using a Riemann solver
276 (Toro 1997). The liquid droplet (or column in 2 dimensions) is initially stagnant located at a distance
277 equal to $1D_0$ from the shock wave, while the passage of the shock triggers its motion and deformation.
278 The pressure outlet boundary condition at the top of the domain patches the value of the temperature
279 and pressure of the neighbouring cell at the boundary, via a UDF, implying transmissive and partially
280 reflective boundary. The computational mesh has increasing cell size in the Y-direction, therefore
281 increasing the numerical diffusion when a wave moves towards the boundary, smoothing the gradients
282 and minimising reflections, thus avoiding the need to move the top boundary at a very large distance.
283 The pressure boundary condition at the right of the domain is non-reflecting, while the one on the left
284 is not in order to avoid discontinuities in the velocity. The grid comprises of rectangular cells applied
285 at two regions of the domain with different grid density (420000 cells in total): i) a rectangle of $8D_0$
286 length and $3D_0$ height with a resolution of 50 cells per radius (cpR), starting from the front of the shock
287 wave and extending $7D_0$ downstream of the droplet, and, ii) the rest of the domain, in which the cell
288 size increases gradually as the distance from the droplet increases, similar to (Meng and Colonius
289 2015). The pressure equation is spatially discretized using the body force weighted scheme, while for

290 the momentum equation the second order upwind scheme (Barth and Jespersen 1989) is utilized. The
291 temporal discretization of all equations is done with the first order implicit scheme, while the time step
292 is such that the acoustic Courant number is equal to 0.8, i.e. below 1, which is common for flows with
293 shock waves (Koukouvinis et al. 2016; Meng and Colonius 2015). Moreover, the VOF equation is solved
294 implicitly and is spatially discretized using an equal blending between first and second order schemes,
295 which gives the best agreement with the results of (Igra and Takayama 2001; Meng and Colonius 2015).
296 The liquid droplet is water with diameter based on (Meng and Colonius 2015), while the surrounding
297 gas is air. The properties of both have been described in equations section and the resulting non-
298 dimensional numbers are presented in Table 1, calculated based on the post-shock properties. In the
299 following sub-sections, the results of the simulation are compared with the experimental data of (Igra
300 and Takayama 2001; Igra and Takayama 2001) and the simulation of (Meng and Colonius 2015).

301

302 **3-D simulation of water droplet breakup**

303 Apart from the well-known 3-D flow features appearing in the aerodynamic breakup of droplets, such
304 as surface instabilities, vortex shedding and formation of liquid sheets (Kaiser et al. 2017; Liu et al.
305 2018; Meng and Colonius 2018), a 3-D simulation is necessary in order to apply the VOF-to-DPM model,
306 which tracks the particles in 3-dimensions following the Lagrangian approach Figure 2 illustrates the
307 3-D computational domain that is utilized for the simulation of droplet breakup at high Ma number.
308 Similar to the domain used in the 2-D simulation (Figure 1), at the top and right boundaries of the
309 computational domain, pressure outlet boundary conditions are applied; while at its left boundary a
310 pressure inlet is assigned. Only 1/8 of the droplet is simulated (45°), while periodic boundary conditions
311 are applied at the front and back of the computational domain. The choice of solving the 1/8 of the
312 droplet using periodic boundary conditions has been made in order to reduce as much as possible the
313 computational resources to make it possible to simulate the examined case with the current numerical
314 tools. Regarding the effect of this choice on the results, limitations of assuming symmetry of the flow

315 field appear in the deformation and breakup of droplets due to turbulence and vortex shedding;
316 nevertheless, these limitations do not affect much the shape of the main droplet (Jain et al. 2018; Liang
317 2016; Stefanitsis et al. 2017). However, as it has been observed in the experiments of (Achenbach
318 1974; Sakamoto and Haniu 1990) and the simulations of (Stefanitsis et al. 2017) vortices in flows
319 around spherical shapes detach periodically from a point at the wake of the droplet that rotates
320 periodically at 45° around an axis that passes through the centre of the sphere; this can possibly affect
321 the trajectory and timing of detachment of the micro-droplets, something that requires the solution
322 of half the droplet in order to fully resolve it. The shock wave is initialized as a step change in the
323 temperature and pressure located at a distance of $1D_0$ from the centre of the droplet. In order to
324 introduce some necessary randomness in the process, the field is initialized with a small “random”
325 instantaneous velocity ($<1/100U_{sh}$), which is calculated based on the turbulent kinetic energy
326 estimated from the κ - ϵ model. The grid cells have a wedge like shape (similar to that of the domain)
327 and it has been created using the 2-D grid of the previous section revolved around the X axis (36
328 partitions in total); this gives a resolution at the interface close to 50cpR. The convective Courant
329 number is equal to 0.5, while the acoustic is 7.85; preliminary 2-D runs have shown that the temporal
330 evolution of droplet shape and velocity do not change much when a smaller time step is used
331 ($Cou_{acoustic} < 1$), therefore saving a lot of computational time in the current 3-D simulation. The spatial
332 discretization of the VOF equation is done using the geo-reconstruct scheme (sharp interface) in
333 contrast to the more diffusive schemes used in the simulation of water column, due to restrictions of
334 the VOF-to-DPM model of FLUENT; the rest of the discretization schemes are the same as in the 2D
335 case.

336 The liquid droplet is water, while the surrounding gas is nitrogen, instead of air in the 2-D case, with
337 properties calculated as described in the sub-section “2-D simulation of water column breakup (model
338 validation)”; the diameter of the droplet is based on (Theofanous et al. 2012). The resulting non-
339 dimensional numbers are calculated based on the post-shock properties and are presented in Table 2.

340

341 **Results and discussion**

342 **2-D simulation of water column breakup (model validation)**

343 **Description of fluid flow**

344 In the numerical simulations of multiphase flows with shock waves, schlieren is commonly used for
345 visualization of the process (Quirk and Karni 1996). The schlieren function is utilized to visualize the
346 density variations of the flow field and is calculated, using eq. (20), as the exponential of the negative,
347 normalized density gradient:

348

$$\varphi = \exp\left(-k \frac{|\nabla\rho|}{\max|\nabla\rho|}\right) \quad (20)$$

349

350 , where k is a scaling parameter equal to 40 for air and 400 for water (Johnsen 2008).

351 The pressure and schlieren contours, as predicted by the simulation, are presented in Figure 3 for
352 various time instances. At the time instance of $t^*=0$, the shock wave front touches the surface of the
353 water droplet, while at $t^*=0.017$ it passes over it and part of it is reflected radially. The droplet starts
354 to deform after some time from the pass of the shockwave, at approximately $t^*=0.171$, taking initially
355 a mushroom-like shape ($t^*=0.444$) and followed by a deformed disk-like shape ($t^*=0.808$). Eventually
356 the breakup occurs with liquid stripping from the periphery of the droplet, which is not clearly visible
357 due to the diffusion of the volume fraction, attributed to the selection of the lower order discretization
358 scheme. This scheme, however, gives results closer to those of (Igra and Takayama 2001; Igra and
359 Takayama 2001; Meng and Colonius 2015).

360 Figure 4 presents the holographic interferograms from the experiment of (Igra and Takayama 2001) as
361 well as the schlieren contours as predicted by the simulation of the current work along with that of
362 (Meng and Colonius 2015), for two time instances. As it is observed from the figure, the shock wave

363 reflection is very similar in the three works for both time instances. The curved black lines correspond
364 to the reflection (R) of the shock-wave in the droplet as well as its diffraction (D). Finally, it should be
365 noted that the time in the experiments is higher compared to both simulations, probably due to a
366 reporting error in (Igra and Takayama 2001) or a misunderstanding of the phrase “time after the
367 interaction between the incident shock wave and the water column” of the original work of (Igra and
368 Takayama 2001), as already discussed thoroughly in (Meng and Colonius 2015).

369 **Results on droplet quantities**

370 Figure 5 presents the temporal evolution of the non-dimensional streamwise and cross-stream
371 deformation, as well as the leading-edge displacement of the droplet, as predicted by the experiment
372 of (Igra and Takayama 2001), the simulation of (Meng and Colonius 2015) and the simulation of the
373 current work ($\alpha=0.5$). As the droplet deforms into an ellipsoid shape, the streamwise deformation
374 gradually decreases with time, while the cross-stream one increases. The leading-edge displacement
375 increases as the droplet moves in the streamwise direction. There is a good agreement between the
376 results of both simulations and the experiment for the streamwise deformation and leading-edge
377 displacement, while a discrepancy is observed with the experiments for the cross-stream deformation;
378 however, the results of the two simulations are close.

379 **3-D simulation of water droplet breakup**

380 **Description of fluid flow**

381 Figure 6 illustrates the temporal evolution of droplet deformation as predicted by the experiment of
382 (Theofanous et al. 2012), the simulation of (Meng and Colonius 2018) and the simulation of the current
383 work. It should be noted that the conditions of this work and those of the experiment are identical,
384 while in the simulation of (Meng and Colonius 2018), the Ma is equal to 1.47 instead of 1.23. Also, the
385 shape in the simulation of (Meng and Colonius 2018) corresponds to the VOF iso-value of 0.01, while
386 in the current work the iso-value of 0.5 is presented. The exact time of the experimental images is not

387 known since they originate from a video, while the time instances of the simulations have been chosen
388 such as to best match the images of the experiments.

389 Similar to the 2-D simulations, the droplet initially deforms into a mushroom-like shape ($t^*=0.274$ and
390 $t^*=0.314$ in the simulation of this work), followed by a disk-like shape ($t^*=0.634$). However, their main
391 difference lies in the breakup initiation time, which is much faster for the 3-D simulation, since micro-
392 droplets are stripped from its periphery as early as $t^*=0.274$. This is attributed to the high velocities at
393 the periphery of the droplet, as shown in Figure 7, which presents in the X-Y plane ($Z=0$) the contour
394 of non-dimensional pressure ($P^*=P/P_{sh}$) at different time instances. The maximum value of the velocity
395 is equal to 1.5, in agreement with the potential flow theory and the simulation of (Meng and Colonius
396 2018). The liquid stripping continues until a large part of the parent droplet has been converted into
397 micro-mist ($t^*=0.634$), something that is also visible in the experiment of (Theofanous et al. 2012). The
398 diameter of these micro-droplets ranges from approximately 25 μm up to 52 μm , which corresponds
399 to the volume equivalent droplet diameter of an interface cell, and it is an input for the model.

400 Nevertheless, in the simulation micro-droplets appear also at the core of the droplet, owing to a conical
401 protuberance appearing axially at the leading edge of the droplet at $t^*=0.234$ and remaining up to
402 $t^*=0.634$, as shown in Figure 8, which presents an enlarged image of the time instance $t^*=0.314$. The
403 latter is attributed to the waves that appear at the surface of the droplet, due to the interaction with
404 the shock wave, as shown in the dimensionless pressure $P^*=P/P_{sh}$ contour of Figure 7: at the time
405 instance of $t^*=0.234$, the pressure is higher at the outer part of the droplet compared to its core, which
406 is the case for the rest of the images, therefore creating the aforementioned protuberance. This is also
407 present in the experiments, starting from the image corresponding to $t^*=0.314$ simulation time and
408 being more visible at $t^*=0.634$, but to a smaller extent. Finally, “wrinkles” appear at the surface of the
409 droplet visible in the simulation at time instance of $t^*=0.234$, which are also present in the experiments,
410 but to a smaller extent.

411 To further understand the procedural deformation and disintegration of the droplet due to the
 412 accumulation of interfacial instabilities, as presented in Figure 6 and Figure 7, an analysis and
 413 explanation of the mechanisms of the droplet break-up is presented in the following section,
 414 examining the sources of vorticity generation on a 3-D slice of the geometry depicted in the previous
 415 section. In particular, the vorticity evolution equation can be expressed as (Green 1995):

416

$$\frac{d\boldsymbol{\omega}}{dt} = (\boldsymbol{\omega} \cdot \nabla)\mathbf{u} - \boldsymbol{\omega}(\nabla \cdot \mathbf{u}) + \frac{1}{\rho^2} \nabla\rho \times \nabla p + \nabla \times \left(\frac{\nabla \cdot \boldsymbol{\tau}}{\rho} \right) + \nabla \times F_\sigma \quad (21)$$

417

418 The first term in the right-hand side represents vortex stretching/tilting, the second term represents
 419 vortex dilation, the third term represents the baroclinic torque, the fourth term expresses vortex
 420 diffusion due to viscous stresses, as defined in eq. 4 and the last term expresses the influence of body
 421 forces. Vortex stretching or tilting is due to the effect of velocity gradient on vorticity; it is a crucial
 422 mechanism in the generation of complex vortical structures and is considered responsible for the
 423 kinetic energy cascade process in turbulence (Wu et al. 2015). Vortex dilation is due to the volumetric
 424 expansion/contraction (the velocity divergence), which describes how fluid compressibility affects the
 425 vorticity. The baroclinic torque occurs due to the different alignment of density and pressure gradients
 426 and is responsible for the formation of Rayleigh-Taylor instabilities. The last term in the present
 427 simulation is only due to the influence of surface tension. Interestingly, as will be shown later, despite
 428 the high Weber number, influence of surface tension is non-negligible, although it contributes to
 429 stabilise the interface.

430 In Figure 9 a comparison of the strength of different factors affecting vorticity evolution is shown, on
 431 a z-slice, similar to the views used in Figure 7, showing the cross-section of the droplet. As observed
 432 from the values of the terms involved, viscous stresses have the lowest contribution in vorticity, being
 433 at least one order of magnitude lower than the other terms. Next, is the contribution of baroclinic
 434 torque, which is entirely located at the near interface region, mainly at the gas side due to the influence

435 of lower gas density in the baroclinic term. The strongest terms are due to manifestation of
 436 compressibility effects (vortex dilation), the turbulent cascade (vortex stretching/tilting) and surface
 437 tension, all terms having a similar order of magnitude. Indeed, based on a similar analysis by (Zandian
 438 et al. 2018), surface tension effect on vorticity scales as $\frac{\sigma \kappa}{\rho \Delta^2}$, which is in the order of 10^{11} s^{-2} for
 439 the present case, assuming a max. curvature of $\kappa=10^6 \text{ m}^{-1}$, density in the order of 10^3 and mesh sizing
 440 of $\sim 25 \mu\text{m}$.

441 An important outcome of this analysis is that viscosity plays a marginal role in the development of the
 442 droplet break-up; indeed, inviscid simulations also confirm this observation (not show in the present
 443 work). Hence, the phenomenon is practically entirely interfacial driven, due to combined Kelvin-
 444 Helmholtz, similar to (Theofanous et al. 2012), and Rayleigh-Taylor instabilities. Another observation
 445 is that, despite the droplet We is ~ 1000 , surface tension will have an effect in stabilising locally
 446 interfacial instabilities, although the destabilising influence of the other terms is much stronger,
 447 contributing to the disintegration of the droplet.

448 **Results on droplet quantities**

449 Figure 10 illustrates the temporal evolution of the dimensionless droplet velocity, displacement and
 450 acceleration, as well as the unsteady drag coefficient, as calculated in the current work and in the
 451 simulation of (Meng and Colonius 2018). The unsteady drag coefficient is calculated using the
 452 momentum balance on the droplet and is given in equation (22). The droplet frontal area is calculated
 453 by assuming a circular area based on the droplet's deformed diameter D_{cr} (assumed equal to D_z),
 454 similar to (Meng and Colonius 2018).

455

$$C_d(t) = \frac{\frac{4}{3} D_0 \varepsilon \frac{dU_d(t)}{dt} \frac{A_f(0)}{A_f(t)}}{(U_{sh} - U_d(t))^2} \quad (22)$$

456

457 Both the velocity and the displacement of the droplet increase with an exponential fashion as the shock
458 wave and the gas flow behind it crosses the droplet and forces it to move. The droplet acceleration
459 starts from zero value, since the droplet is initially stagnant, while it increases rapidly due to the droplet
460 being in motion from stagnation; after a small fluctuation at the initial stages of the simulation owing
461 to the unsteady flow field, it eventually increases gradually as the droplet accelerates steadily. The
462 drag coefficient experiences a similar decline at the initial stages of the simulation; however, it
463 increases only slightly followed by a decrease at the later stages of the simulation. This is attributed to
464 the increase of the frontal area of the droplet ($A_f(t)/A_f(0)$) as it deforms in the cross-stream direction.
465 The results from the simulation of (Meng and Colonius 2018) follow a similar trend, while being slightly
466 higher compared to the simulations of this study, probably due to the higher Ma number (1.47
467 compared to 1.23).

468 Finally, the temporal evolution of droplet deformation in both axes (streamwise and cross-stream) and
469 surface area are presented in Figure 11. The cross-stream deformation and surface area increase as
470 the droplet takes an ellipsoid shape, while the streamwise deformation decreases followed by a slight
471 increase at the final stages of the simulation; this is attributed to the liquid sheets formed at the
472 periphery of the droplet (Figure 6 at $t^*=0.634$), which are also reported in the works of (Kaiser et al.
473 2017; Meng and Colonius 2018). The fluctuation in the value of cross-stream deformation at the time
474 instance of approximately 0.5 is attributed to the stripping of the micro-droplets from its periphery,
475 something that results in the decrease of the size of the parent droplet.

476 **Conclusions**

477 In the current work 2-D planar (column) and 3-D simulations were performed for droplets exposed to
478 gas flows of Ma numbers ranging from 1.23 up to 1.46. The CFD model solves the compressible Navier-
479 Stokes equations, the energy equation, the VOF equation along with two equations of state to model
480 the density variations of the two phases. In addition, in the 3-D simulation the VOF-to-DPM model of

481 FLUENT was utilized, which switches from VOF to DPM when certain user-defined criteria are met, in
482 order to capture the appearance of micro-droplets detached from the parent droplet.
483 The results of the 2-D simulation are compared against published experimental (Igra and Takayama
484 2001) and numerical (Meng and Colonius 2015) data and good qualitative agreement is observed for
485 the pressure and numerical schlieren contours. In addition, the quantitative results for the streamwise
486 deformation and the leading-edge displacement are also in good agreement with experiments.
487 However, a discrepancy was observed for the cross-stream deformation.
488 Regarding the 3-D simulation, the predicted temporal evolution of droplet shape was similar to that of
489 the experiments of (Theofanous et al. 2012). The simulation predicted the appearance of micro-
490 droplets at the periphery of the droplet as well as surface instabilities (K-H and R-T) similar to the
491 experiments. Finally, results for the droplet deformation and surface area were presented and a steady
492 increase in the surface area and cross-stream deformation was observed, as the drop takes an ellipsoid
493 shape, while the streamwise deformation initially decreases followed by an increase at the later stages
494 of the simulations, due to the formation of liquid sheets at the periphery of the droplet.

495

496 **Data availability statement**

497 All data, models, or code that support the findings of this study are available from the corresponding
498 author upon reasonable request.

499

500 **Acknowledgements**

501 Financial support from the MSCA-ITN-ETN of the European Union's H2020 programme, under REA
502 grant agreement n. 675676 is acknowledged.

503

504 **Notation**

Roman symbols

A_f	Frontal area [m ²]
c	Speed of sound [m/s]
C_d	Drag coefficient [-]
Cou	Courant number [-]
C_p	Specific heat [J/kgK]
D	Droplet diameter or deformation [m]
E	Energy [J]
F	Force [N]
h	Enthalpy [J/kg]
K	Bulk modulus [bar]
k	Scaling parameter [-]
Ma	Mach number [-]
m	Mass [kg]
\vec{n}	Free-surface unit normal [-]
Oh	Ohnesorge number [-]
P	Pressure [Pa]
Re	Reynolds number [-]
S	Surface area [m ²]
T	Temperature [K]
t	Time [s]
t_{shear}	Shear breakup timescale [s]
U, u	Velocity [m/s]
V	Volume [m ³]
v	Specific volume [m ³ /kg]

ρ	Density [kg/m ³]
σ	Surface tension [N/m]
τ_r	Droplet relaxation time [s]
ϕ	Schlieren function [-]

Subscripts/Superscripts

*	Non-dimensional quantity
O	Initial
cm	Center of mass
cr	Cross-stream
d	Droplet
g	Gas
L	Liquid
mag	Magnitude
sh	Post-shock quantity
str	Streamwise
$press$	Pressure
ref	Reference
vol	Volumetric

Abbreviations

$CLSVOF$	Coupled Level-Set with VOF
DPM	Discrete phase model
EoS	Equation of state
KH	Kelvin-Helmholtz
LE	Leading-edge
LS	Level set

We	Weber number [-]	RT	Rayleigh-Taylor
Greek symbols		RTP	Rayleigh-Taylor piercing
α	Volume fraction [-]	SIE	Shear induced entrainment
ε	Density ratio [-]	UDF	User-defined function
μ	Dynamic viscosity [kg/(m·s)]	VOF	Volume of fluid

505

506 References

- 507 "ANSYS®FLUENT Theory Guide, 2014, Release 16.0."
508 Achenbach, E. 1974. "Vortex shedding from spheres." *Journal of Fluid Mechanics*, 62(02), 209-221.
509 Allaire, G., Clerc, S., and Kokh, S. 2002. "A five-equation model for the simulation of interfaces between
510 compressible fluids." *Journal of Computational Physics*, 181(2), 577-616.
511 Barth, T., and Jespersen, D. 1989. "The design and application of upwind schemes on unstructured meshes." *Proc.,
512 27th Aerospace sciences meeting*, 366.
513 Bo Shen, Q. Y., Oliver Tiedje, Joachim Domnick 2019. "Simulation of the primary breakup of non-Newtonian liquids
514 at a high-speed rotary bell atomizer for spray painting processes using a VOF-Lagrangian Hybrid Model." *29th European Conference on Liquid Atomization and Spray Systems, ILASSParis*.
515 Boiko, V., Papyrin, A., and Poplavskii, S. 1987. "Dynamics of droplet breakup in shock waves." *Journal of applied
516 mechanics and technical physics*, 28(2), 263-269.
517 Boiko, V., and Poplavski, S. 2009. "On the dynamics of drop acceleration at the early stage of velocity relaxation in
518 a shock wave." *Combustion, Explosion, and Shock Waves*, 45(2), 198-204.
519 Chang, C.-H., Deng, X., and Theofanous, T. G. 2013. "Direct numerical simulation of interfacial instabilities: a
520 consistent, conservative, all-speed, sharp-interface method." *Journal of Computational Physics*, 242, 946-
521 990.
522 Chang, C.-H., and Liou, M.-S. 2007. "A robust and accurate approach to computing compressible multiphase flow:
523 Stratified flow model and AUSM+-up scheme." *Journal of Computational Physics*, 225(1), 840-873.
524 Engel, O. G. 1958. "Fragmentation of Waterdrops in the Zone Behind an Air Shock, J. Research Nat'l." *Bur. Stds*,
525 60(245), 19.
526 G. Strotos, I. M., N. Nikolopoulos, K. Papadopoulos, A. Theodorakakos, M. Gavaises. 2015. "Performance of VOF
527 methodology in predicting the deformation and breakup of impulsively accelerated droplets." *ICLASS
528 2015, 13th Triennial International Conference on Liquid Atomization and Spray Systems, August 23-
529 27Tainan, Taiwan*.
530 Gor, G. Y., Siderius, D. W., Shen, V. K., and Bernstein, N. 2016. "Modulus–pressure equation for confined fluids." *The
531 Journal of chemical physics*, 145(16), 164505.
532 Green, B. 1995. *Fluid Vortices*, Springer Netherlands.
533 Guan, B., Liu, Y., Wen, C.-Y., and Shen, H. 2018. "Numerical Study on Liquid Droplet Internal Flow Under Shock
534 Impact." *AIAA Journal*, 56(9), 3382-3387.
535 Guildenbecher, D. R., López-Rivera, C., and Sojka, P. E. 2009. "Secondary atomization." *Experiments in Fluids*,
536 46(3), 371-402.
537 Hébert, D., Rullier, J.-L., Chevalier, J.-M., Bertron, I., Lescoute, E., Virost, F., and El-Rabii, H. 2019. "Investigation
538 of mechanisms leading to water drop breakup at Mach 4.4 and Weber numbers above 105." *SN Applied
539 Sciences*, 2(1), 69.
540 Hirt, C. W., and Nichols, B. D. 1981. "Volume of fluid (VOF) method for the dynamics of free boundaries." *Journal
541 of Computational Physics*, 39(1), 201-225.
542 Igra, D., and Takayama, K. 2001. "Numerical simulation of shock wave interaction with a water column." *Shock
543 Waves*, 11(3), 219-228.
544 Igra, D., and Takayama, K. 2001. "A study of shock wave loading on a cylindrical water column." *Report of the
545 Institute of Fluid Science, Tohoku University*, 13, 19-36.
546 Ivings, M., Causon, D., and Toro, E. 1998. "On Riemann solvers for compressible liquids." *International Journal for
547 Numerical Methods in Fluids*, 28(3), 395-418.
548 Jain, S. S., Tyagi, N., Prakash, R. S., Ravikrishna, R., and Tomar, G. 2018. "Secondary breakup of drops at
549 moderate Weber numbers: Effect of Density ratio and Reynolds number." *arXiv preprint arXiv:1803.02989*.
550 Johnsen, E. 2008. "Numerical simulations of non-spherical bubble collapse: With applications to shockwave
551 lithotripsy." California Institute of Technology.

553 Joseph, D., Beavers, G., and Funada, T. 2002. "Rayleigh–Taylor instability of viscoelastic drops at high Weber
554 numbers." *Journal of Fluid Mechanics*, 453, 109-132.

555 Joseph, D. D., Belanger, J., and Beavers, G. 1999. "Breakup of a liquid drop suddenly exposed to a high-speed
556 airstream." *International Journal of Multiphase Flow*, 25(6-7), 1263-1303.

557 Kaiser, J., Adami, S., and Adams, N. A. 2017. "Direct Numerical Simulation of Shock-Induced Drop Breakup with a
558 Sharp-Interface-Method." *Proc., Symposium on Turbulence and Shear Flow Phenomena [TSFP10]*.

559 Koukouvini, P., Gavaises, M., Supponen, O., and Farhat, M. 2016. "Numerical simulation of a collapsing bubble
560 subject to gravity." *Physics of Fluids*, 28(3), 032110.

561 Koukouvini, P., Roncero, A. V., Rodriguez, C., Gavaises, M., and Picket, L. 2020. "High pressure/high
562 temperature multiphase simulations of dodecane
563 injection to nitrogen: application on ECN Spray-A (under review)." *FUEL*.

564 Lafaurie, B., Nardone, C., Scardovelli, R., Zaleski, S., and Zanetti, G. 1994. "Modelling Merging and Fragmentation
565 in Multiphase Flows with SURFER." *Journal of Computational Physics*, 113(1), 134-147.

566 Lemmon, E. 2013. "NIST Standard Reference Database 23, Reference Fluid Thermodynamic and Transport
567 Properties (REFPROP), version 9.1, National Institute of Standards and Technology."

568 Liang, C. 2016. "Computational methods for the investigation of liquid drop phenomena in external gas flows." PhD
569 Open Access Dissertation, Michigan Technological University.

570 Liou, M.-S., Chang, C.-H., Chen, H., and Hu, J.-J. 2009. "Numerical study of shock-driven deformation of
571 interfaces." *Shock Waves*, Springer, 919-924.

572 Liu, N., Wang, Z., Sun, M., Wang, H., and Wang, B. 2018. "Numerical simulation of liquid droplet breakup in
573 supersonic flows." *Acta Astronautica*, 145, 116-130.

574 Liu, Z., and Reitz, R. D. 1997. "An analysis of the distortion and breakup mechanisms of high speed liquid drops."
575 *International Journal of Multiphase Flow*, 23(4), 631-650.

576 Malgarinos, I., Nikolopoulos, N., and Gavaises, M. 2015. "Coupling a local adaptive grid refinement technique with
577 an interface sharpening scheme for the simulation of two-phase flow and free-surface flows using VOF
578 methodology." *Journal of Computational Physics*, 300, 732-753.

579 Malgarinos, I., Nikolopoulos, N., and Gavaises, M. 2016. "A numerical study on droplet-particle collision dynamics."
580 *International Journal of Heat and Fluid Flow*, 61, Part B, 499-509.

581 Malgarinos, I., Nikolopoulos, N., and Gavaises, M. 2017. "Numerical investigation of heavy fuel droplet-particle
582 collisions in the injection zone of a Fluid Catalytic Cracking reactor, Part I: Numerical model and 2D
583 simulations." *Fuel Processing Technology*, 156, 317-330.

584 Malgarinos, I., Nikolopoulos, N., and Gavaises, M. 2017. "Numerical investigation of heavy fuel droplet-particle
585 collisions in the injection zone of a Fluid Catalytic Cracking reactor, part II: 3D simulations." *Fuel
586 Processing Technology*, 156, 43-53.

587 Malgarinos, I., Nikolopoulos, N., Marengo, M., Antonini, C., and Gavaises, M. 2014. "VOF simulations of the contact
588 angle dynamics during the drop spreading: Standard models and a new wetting force model." *Advances
589 in Colloid and Interface Science*, 212, 1-20.

590 Meng, J., and Colonius, T. 2015. "Numerical simulations of the early stages of high-speed droplet breakup." *Shock
591 Waves*, 25(4), 399-414.

592 Meng, J. C., and Colonius, T. 2018. "Numerical simulation of the aerobreakup of a water droplet." *Journal of Fluid
593 Mechanics*, 835, 1108-1135.

594 Meng, J. C. C. 2016. "Numerical simulations of droplet aerobreakup." California Institute of Technology.

595 Menon, E. S. 2014. *Transmission pipeline calculations and simulations manual*, Gulf Professional Publishing.

596 Morsi, S., and Alexander, A. 1972. "An investigation of particle trajectories in two-phase flow systems." *Journal of
597 Fluid Mechanics*, 55(2), 193-208.

598 Nicholls, J. A., and Ranger, A. A. 1969. "Aerodynamic shattering of liquid drops." *AIAA Journal*, 7(2), 285-290.

599 Perry, R. H., and Green, D. W. 1999. *Perry's Chemical Engineers' Handbook-Cdrom*, McGraw Hill.

600 Quirk, J. J., and Karni, S. 1996. "On the dynamics of a shock–bubble interaction." *Journal of Fluid Mechanics*, 318,
601 129-163.

602 Sakamoto, H., and Haniu, H. 1990. "A study on vortex shedding from spheres in a uniform flow." *ASME,
603 Transactions, Journal of Fluids Engineering*, 112, 386-392.

604 Sonntag, R. E., Van Wylen, G. J., and Borgnakke, C. 2008. *Fundamentals of thermodynamics*, Wiley.

605 Stefanitsis, D., Malgarinos, I., Strotos, G., Nikolopoulos, N., Kakaras, E., and Gavaises, M. 2017. "Numerical
606 investigation of the aerodynamic breakup of Diesel and heavy fuel oil droplets." *International Journal of
607 Heat and Fluid Flow*, 68, 203-215.

608 Stefanitsis, D., Malgarinos, I., Strotos, G., Nikolopoulos, N., Kakaras, E., and Gavaises, M. 2017. "Numerical
609 investigation of the aerodynamic breakup of Diesel droplets under various gas pressures." *28th
610 Conference on Liquid Atomization and Spray Systems (ILASS-Europe 2017)*Valencia, Spain.

611 Stefanitsis, D., Malgarinos, I., Strotos, G., Nikolopoulos, N., Kakaras, E., and Gavaises, M. 2018. "Numerical
612 investigation of the aerodynamic breakup of droplets in tandem." *International Journal of Multiphase Flow*.

613 Stefanitsis, D., Strotos, G., Nikolopoulos, N., and Gavaises, M. 2019. "Numerical investigation of the aerodynamic
614 breakup of a parallel moving droplet cluster." *International Journal of Multiphase Flow*, 121, 103123.

615 Stefanitsis, D., Strotos, G., Nikolopoulos, N., Kakaras, E., and Gavaises, M. 2018. "Numerical examination of the
616 aerodynamic breakup of droplets in chain formation." *14th Triennial International Conference on Liquid
617 Atomization and Spray Systems (ICLASS 2018)*Chicago, USA.

618 Stefanitsis, D., Strotos, G., Nikolopoulos, N., Kakaras, E., and Gavaises, M. 2019. "Improved droplet breakup
619 models for spray applications." *International Journal of Heat and Fluid Flow*, 76, 274-286.
620 Strotos, G., Malgarinos, I., Nikolopoulos, N., and Gavaises, M. 2016. "Aerodynamic breakup of an n-decane droplet
621 in a high temperature gas environment." *Fuel*, 185, 370-380.
622 Strotos, G., Malgarinos, I., Nikolopoulos, N., and Gavaises, M. 2016. "Numerical investigation of aerodynamic
623 droplet breakup in a high temperature gas environment." *Fuel*, 181, 450-462.
624 Strotos, G., Malgarinos, I., Nikolopoulos, N., and Gavaises, M. 2016. "Predicting droplet deformation and breakup
625 for moderate Weber numbers." *International Journal of Multiphase Flow*, 85, 96-109.
626 Strotos, G., Malgarinos, I., Nikolopoulos, N., and Gavaises, M. 2016. "Predicting the evaporation rate of stationary
627 droplets with the VOF methodology for a wide range of ambient temperature conditions." *International
628 Journal of Thermal Sciences*, 109, 253-262.
629 Surov, V. 1995. "Numerical modeling of the interaction of a strong shock wave with liquid drops." *Journal of applied
630 mechanics and technical physics*, 36(3), 354-359.
631 Sutherland, W. 1893. "LII. The viscosity of gases and molecular force." *The London, Edinburgh, and Dublin
632 Philosophical Magazine and Journal of Science*, 36(223), 507-531.
633 Theofanous, T., and Li, G. 2008. "On the physics of aerobreakup." *Physics of Fluids*, 20(5), 052103.
634 Theofanous, T., Mitkin, V., Ng, C., Chang, C., Deng, X., and Sushchikh, S. 2012. "The physics of aerobreakup. II.
635 Viscous liquids." *Physics of Fluids*, 24(2), 022104.
636 Theofanous, T. G., Li, G. J., and Dinh, T. N. 2004. "Aerobreakup in Rarefied Supersonic Gas Flows." *Journal of
637 Fluids Engineering*, 126(4), 516-527.
638 Toro, E. F. 1997. "The Riemann Problem for the Euler Equations." *Riemann Solvers and Numerical Methods for
639 Fluid Dynamics: A Practical Introduction*, E. F. Toro, ed., Springer Berlin Heidelberg, Berlin, Heidelberg,
640 115-157.
641 Wagner, W., and Pruß, A. 2002. "The IAPWS formulation 1995 for the thermodynamic properties of ordinary water
642 substance for general and scientific use." *Journal of physical and chemical reference data*, 31(2), 387-
643 535.
644 Wierzba, A., and Takayama, K. 1988. "Experimental investigation of the aerodynamic breakup of liquid drops." *AIAA
645 Journal*, 26(11), 1329-1335.
646 Wu, J.-Z., Ma, H.-Y., and Zhou, M.-D. 2015. *Vortical Flows*, Springer-Verlag Berlin Heidelberg.
647 Xiao, F., Wang, Z., Sun, M., Liu, N., and Yang, X. 2017. "Simulation of drop deformation and breakup in supersonic
648 flow." *Proceedings of the Combustion Institute*, 36(2), 2417-2424.
649 Yi, X., Zhu, Y., and Yang, J. 2017. "On the Early-Stage Deformation of Liquid Drop in Shock-Induced Flow." *Proc.,
650 30th International Symposium on Shock Waves 2*, Springer, 1269-1273.
651 Yoshida, T., and Takayama, K. 1990. "Interaction of liquid droplets with planar shock waves." *Journal of Fluids
652 Engineering*, 112(4), 481-486.
653 Zandian, A., Sirignano, W. A., and Hussain, F. 2018. "Understanding liquid-jet atomization cascades via vortex
654 dynamics." *Journal of Fluid Mechanics*, 843, 293-354.
655

656 Table 1: Droplet diameter and non-dimensional numbers of the 2-D simulation of droplet breakup.

D_0 (m)	We	Re	Oh	ϵ	Ma
$4.8 \cdot 10^{-3}$	7355	107069	0.0017	831	1.47

657

658

659 Table 2: Droplet diameter and non-dimensional numbers of the 3-D simulation of droplet breakup.

D_0 (m)	We	Re	Oh	ϵ	Ma
$2.4 \cdot 10^{-3}$	780	191169	0.0024	617	1.24

660

661

662 **List of figures**

663 Figure 1: Computational domain utilized for the 2-D planar simulation of column breakup.

664 Figure 2: Computational domain utilized for the 3-D simulation of droplet breakup.

665 Figure 3: Pressure and Schlieren contours from the 2-D simulation of droplet breakup ($\alpha=0.5$). Flow is
666 from left to right.

667 Figure 4: a) Holographic interferograms from the experiment of (Igra and Takayama, 2001a) and
668 numerical schlieren images from the simulations of b) (Meng and Colonius, 2015) and c) the current
669 study, at two time instances. Flow is from left to right.

670 Figure 5: Temporal evolution of the non-dimensional a) streamwise deformation, b) cross-stream
671 deformation and c) leading-edge displacement of the droplet, as predicted by the experiment of (Igra
672 and Takayama, 2001a), the simulation of (Meng and Colonius, 2015) and the simulation of the current
673 work ($\alpha=0.5$).

674 Figure 6: Temporal evolution of droplet deformation as predicted by a) the experiment of (Theofanous
675 et al., 2012), b) the simulation of (Meng and Colonius, 2018) ($\alpha=0.01$) and c) the simulation of the
676 current work ($\alpha=0.5$). Flow is from left to right.

677 Figure 7: Contour in the X-Y plane ($Z=0$) of the non-dimensional pressure. Flow is from left to right.

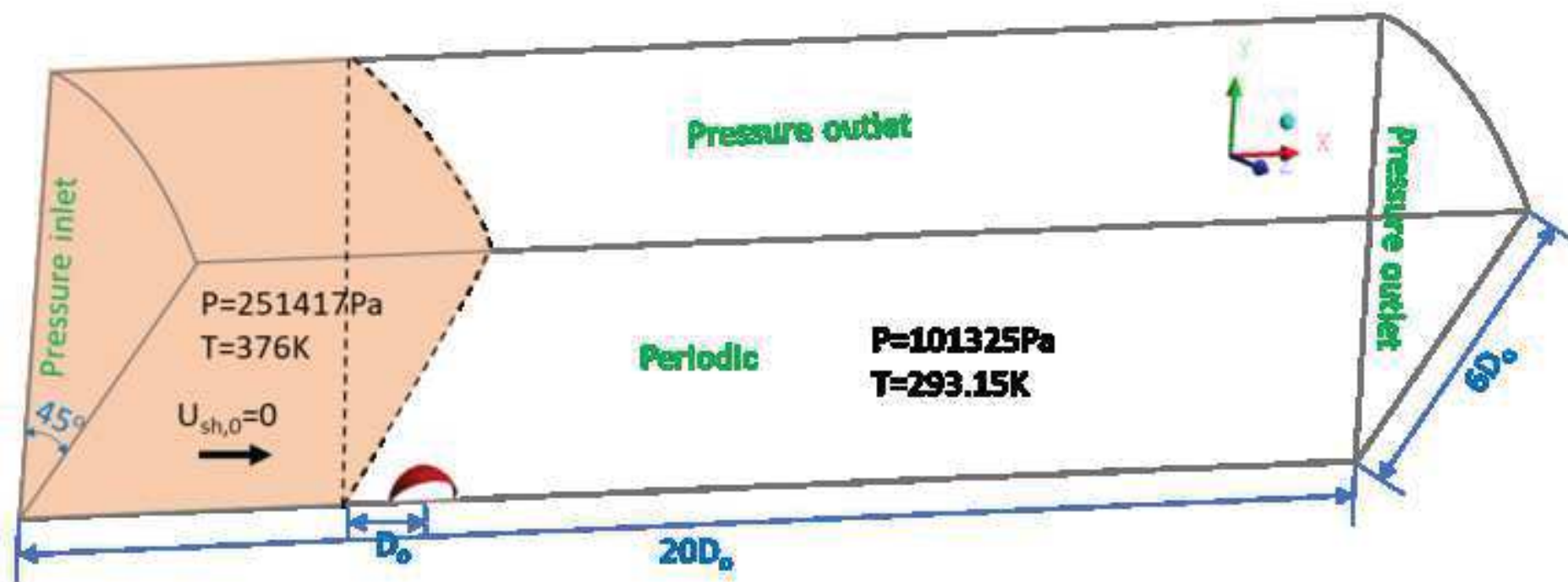
678 Figure 8: Conical protuberance visible at the leading edge of the droplet ($t^*=0.314$).

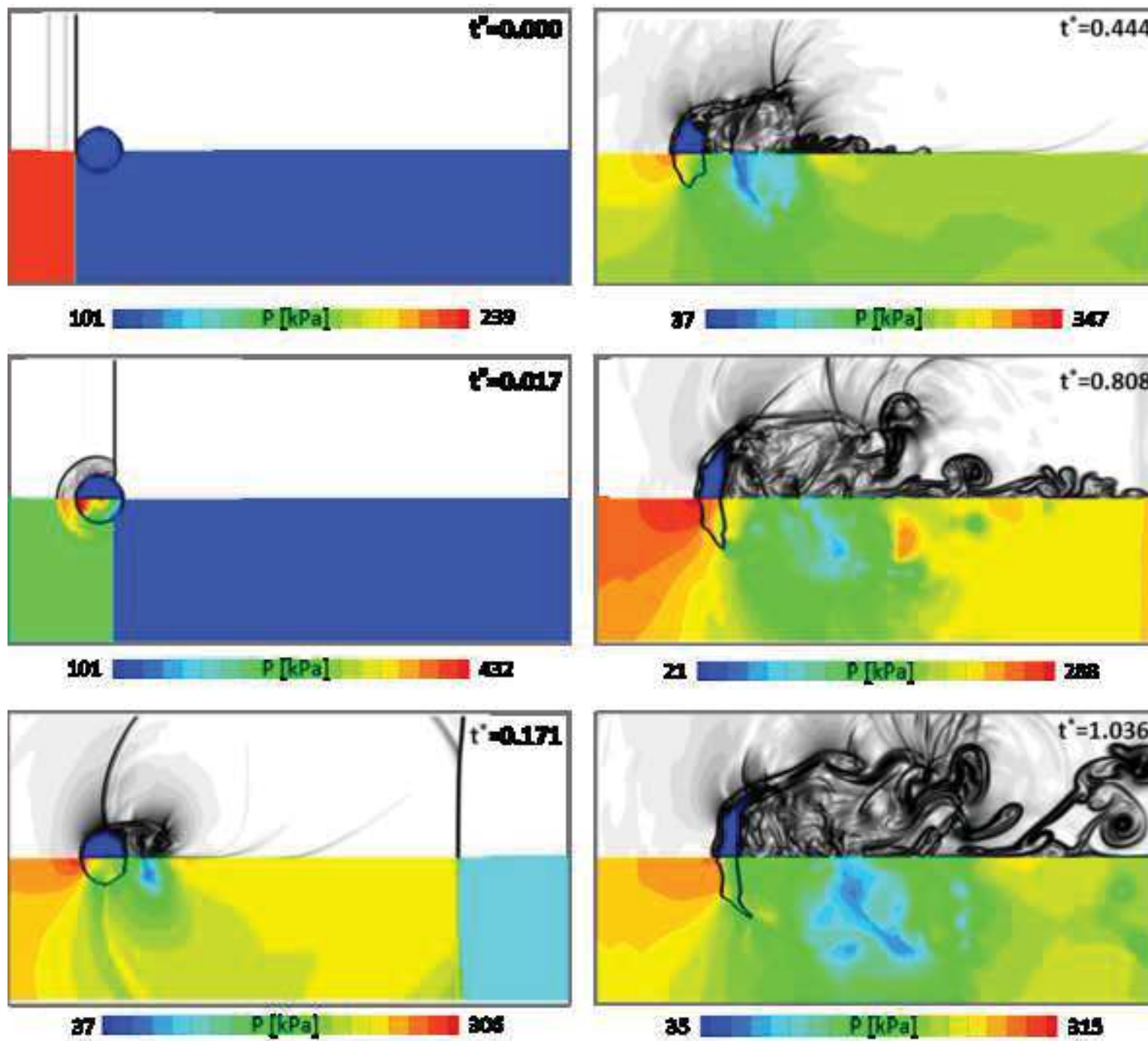
679 Figure 9. Contribution of different vorticity generation mechanisms at a slice showing the droplet
680 cross-section. (a) vortex stretching/tilting, (b) vortex dilation, (c) baroclinic torque, (d) viscous stresses
681 and (e) body forces due to surface tension. All values are in the same units of vorticity generation rate
682 (s^{-2}). Note that the body force term actually contributes to dampen interfacial instabilities. The thick
683 black line shows the droplet interface (volume fraction 0.5).

684 Figure 10: Temporal evolution of the dimensionless droplet a) velocity, b) displacement and c)
685 acceleration, as well as d) the unsteady drag coefficient, as calculated in the current work and in the
686 simulation of (Meng and Colonius, 2018).

687 Figure 11: Temporal evolution of droplet a) deformation in both axes (streamwise and cross-stream)
688 and b) surface area.



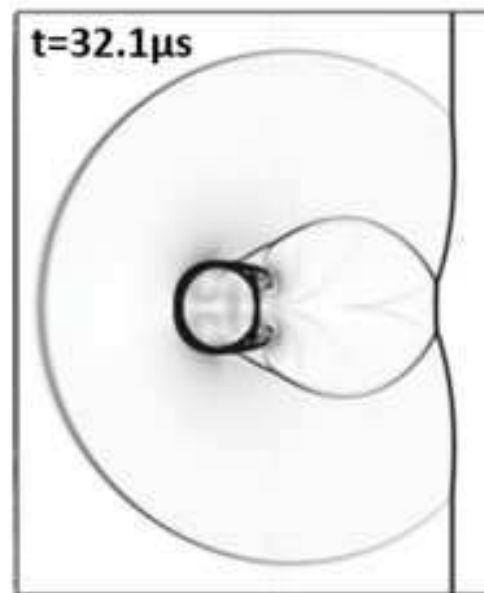
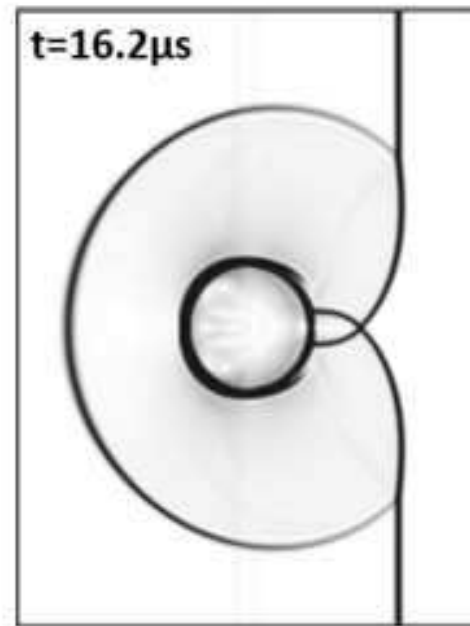




a) Experiment of Igra and Takayama



b) Simulation of Meag and Colonius



c) Current simulation

